Taking control of charge transfer : strategic design for solar cells

Monti, Adriano

Chapter 4

Crucial Role of Nuclear Dynamics in Heterogeneous Electron Transfer

4.0. ABSTRACT

This chapter investigates the process of electron injection from a terrylene-based chromophore to a TiO_2 semiconductor bridged by a recently proposed phenyl-amide-phenyl molecular rectifier. The mechanism of electron transfer is studied by means of quantum electron dynamics simulations using an extended Hückel Hamiltonian. Prior to the quantum dynamics simulations, nuclear dynamics trajectories are calculated separately through ab initio Molecular Dynamics. It is found that the inclusion of the nuclear motion, in a coupled quantum-classical framework, opens a channel for coherent long range directional photoinduced electron transfer. This nonadiabatic process occurs between near-degenerate donor and acceptor states. In particular, the fluctuations of the dihedral angle between the terrylene and the phenyl ring modulate the localization and thus the electronic coupling between the donor and acceptor states. The electron propagation shows characteristic oscillatory features that correlate with interatomic distance fluctuations in the bridge. Hence the system acts as a "phonon antenna" to specific vibrational modes obtained in the ab initio molecular dynamics beforehand to drive the process. The understanding of coherent effects is important for the design of functional dyes with low-loss injection and rectification properties.

This chapter is based on the publication:

Monti, A.; Negre, C.F.A.; Batista, V.S.; Rego, L.C.G.; de Groot, H.J.M.; Buda, F. Crucial Role of Nuclear Dynamics for Electron Injection in a Dye-Semiconductor Complex. *J. Phys. Chem. Lett.* **2015**, 6, 2393-2398.

4.1. INTRODUCTION

Environmentally friendly and cost-effective dye-sensitized solar cells (DSSCs) are a potential alternative to silicon-based photovoltaics for solar energy conversion, can be equipped with molecular catalysts for direct conversion and storage of solar energy into fuel, and have been the subject of extensive research[1–5]. In DSSC devices a semiconductor electrode is functionalized with a (molecular) chromophore absorbing visible light. The photoexcitation induces heterogeneous electron transfer (ET) from the dye into the semiconductor conduction band (CB), while an electrolyte shuttles electrons from the counter electrode to regenerate the oxidized dye.

Despite considerable improvement achieved in recent years, DSSCs performances have not reached energy conversion yields and efficiency levels that are necessary to render them competitive with silicon-based solar cells. Higher efficiencies can be attained by increasing the light harvesting properties of the solar cell, by decreasing internal energy losses or by optimizing conditions for fast electron injection.

A major obstacle hampering the performance of DSSC devices is represented by the internal losses from recombination between the electron injected into the semiconductor and the hole on the oxidized dye[6]. In a converging approach to design more efficient devices, several groups have investigated the effect of specific cell parameters for enhancing electron injection and reducing recombination losses, such as length and nature of the bridges[7–10], the chemical structure of the anchor groups[11] and the redox potential of the electrolyte[12]. In addition, detailed investigations of the molecular mechanisms at the dye/semiconductor interface[13–18] have revealed the importance of nonadiabatic dynamics for charge separation and recombination[19–21].

Recently, Batista and coworkers proposed the use of a molecular rectifier[22] composed of two phenyl rings coupled through an amide bond to prevent back electron transfer (see AM molecule in **Scheme 4.1a**). This molecule acts as a rectifier when used as a molecular wire or as a linker-chromophore in a solar cell device[23,24]. In these previous works it has been shown that the rectifying properties of AM can be rationalized in terms of the asymmetric charge distribution of the frontier molecular orbitals. Used as a molecular bridge between a dye and a semiconductor, a rectifying AM linker could increase the DSSC efficiency by decreasing the electron-hole recombination rate.

To investigate the role of AM in the electron injection process, we use it to bridge an amine-functionalized terrylene antenna (T) and a titanium dioxide (TiO_2) anatase surface (T-AM-TiO_2, **Scheme 4.1b**). Terrylene is a well characterized molecule that absorbs within the visible spectrum (~580 nm) and has an excited state lifetime on

the ns time scale[25,26]. Recently this molecule has been also used as electron donor for TiO_2 based DSSC[27]. TiO_2, in turn, is a semiconductor material widely used as an electron collector in DSSC. This oxide is known for its stability, its high surface area for dye loading, and its high electron collection efficiency; additionally, its bands allow efficient electron transfer from most of the commercially available dyes[6]. The anchoring of the dye onto TiO_2 is achieved through a carboxylic acid group in a bidentate bridging mode (**Scheme 4.1b**).

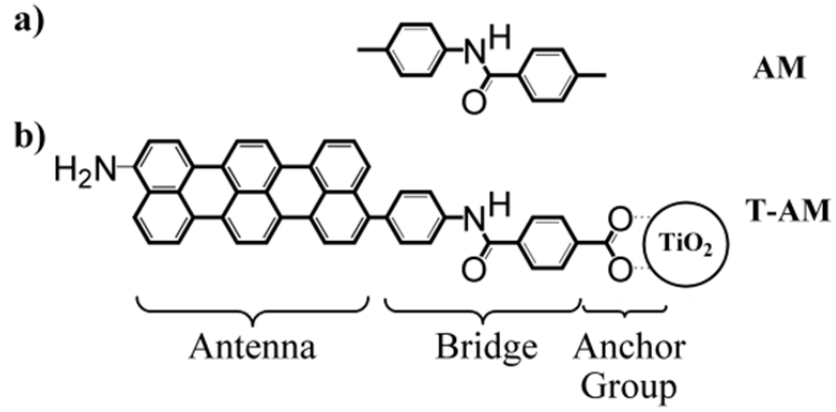

Scheme 4.1. Chemical structure of the molecular rectifier AM (a), and of the T-AM dye (b). The anchoring of the chromophore to the TiO_2 semiconductor through a carboxylic acid group (anchor group), leads to the formation of the T-AM-TiO_2 system.

To provide insight for the design of more efficient charge separators, I have investigated the quantum dynamics of electron injection coupled to thermal nuclear motion in a coupled quantum-classical framework where the nonadiabatic connection between successive molecular conformations is carried out through the diabatic atomic orbitals base. The semi-classical simulations show that the system is able to selectively couple to specific modes from a nuclear dynamics trajectory to open a rectifying electron injection channel in the T-AM-TiO_2 system by a coherent superposition of states. This mechanism is fundamentally different from a semiconductor junction, since the unidirectional conversion of the initial excited state on the chromophore is due to coherent mixing with a charge transfer state between the chromophore and the TiO_2, which does not rely only on an energy gradient, but requires in addition strong electronic coupling from nearly degenerate exciton and charge transfer states. The vibronic coupling to normal modes localized at the interface between the antenna and the semiconductor drives the process. These results support recent findings on the importance of coherent vibronic coupling during photo-induced charge separation processes for both natural and artificial light-harvesting systems[16,28–34].

4.2. METHODS AND COMPUTATIONAL DETAILS

The electronic properties of the systems are quantum mechanically described by means of a tight-binding Hamiltonian based on the extended Hückel (EH) theory[35,36] (see also chapter 2 of this thesis).

The EH method implementation used here, employs as basis set of K nonorthogonal Slater-type orbitals (STO) centered at the position of the respective atom in the system. A set of adiabatic molecular orbitals (MO) is constructed as linear combinations of the STO atomic orbitals (AO) according to $\psi = \sum_{\nu=1}^{K} c_\nu \varphi_\nu$. It follows that the coefficients c_ν are obtained by solving the generalized eigenvalue equations $\sum_{\nu=1}^{K} c_\nu \left(H_{\nu\mu} - \varepsilon S_{\nu\mu}\right) = 0,\ \forall \mu = 1, K.$ Here $H_{\nu\mu}$ and $S_{\nu\mu}$ are respectively the electronic Hamiltonian and the overlap matrix elements in the AO basis representation, while ε is the corresponding eigenvalue. The diagonal elements $H_{\nu\nu}$ are called Coulomb integrals. The value of each of them is assigned through parametrization and represents approximately the valence state oxidation potential of the atomic orbitals ν. The off-diagonal elements $H_{\nu\mu} = \frac{1}{2}\, k_{\nu\mu}\left(H_{\nu\nu} + H_{\mu\mu}\right) S_{\nu\mu}$ (or bond integrals) represent the energy of the electron in the region where the two atomic orbitals ν and μ overlap ($S_{\nu\mu}$). $k_{\nu\mu}$ are the modified empirical Wolfsberg-Helmholz parameters[36,37]. The matrix elements of the tight-binding EH Hamiltonian are therefore dependent on three semiempirical parameters: $H_{\nu\nu}$, $k_{\nu\mu}$ and the effective charge of the nucleus (ζ) embedded in the definition of the STOs.

In standard EH methods, these parameters are subject to the following approximations: i) the Coulomb integrals are approximated with the oxidation potential of the valence-shell atomic orbital; ii) no distinction based on the atom chemical environment is made for the parametrization of the AOs; iii) $k_{\nu\mu}$ is assumed equal to 1.75. These approximations can strongly affect the outcome of the calculations, depending on the systems under investigation. To overcome these problems, for our investigation we use parameters previously optimized against experimental and DFT results. Additionally, the molecular environment is also considered during optimization through the enlargement of the AOs basis set. The optimization procedure is described in the next section 4.2.1.

4.2.1. Optimization of the Extended Hückel parameters

Initially, the density of states (DOS) for the (110) surface of anatase is obtained with the standard EH parameters[38] imposing periodic boundary conditions along the

[101] and the [010] directions. For the calculation of the isolated TiO_2 surface, as well as for the functionalized one, an orthorhombic supercell with lattice parameters *a*=10.239 Å, *b*=15.137 Å and *c*=40 Å is used. The standard EH calculation estimates the lower edge of the TiO_2 conduction band (CB) at -10 eV.

At the same time, the T-AM chromophore geometry is optimized in its ground state at the DFT level, using the exchange correlation functional B3LYP[39] coupled with the Gaussian type basis set cc-pVDZ. The DFT calculations are performed with the Gaussian09 software package[40]. This computational set-up has already been proved accurate in describing the electronic properties of a similar terrylene/TiO_2 based DSSC device[27].

Although it is experimentally difficult to obtain an accurate estimate for this parameter, -4.0 eV (vs. vacuum) is commonly accepted as an appropriate value for the edge of the TiO_2 CB[27,41]. Consequently, in order to obtain the energy gradient with respect to the semiconductor CB calculated with the EH method (-10 eV), the DFT frontier molecular orbital (FMO) energy values are down shifted by 6 eV. These corrected energies are used as target values for the optimization of the EH parameters. The optimization is performed by minimizing the cost function f of the form

$$f(\{\zeta\},\{H_{vv}\},\{k\}) = \sum_{j=1}^{M^{\mathrm{CONSTR}}} \omega_j \left[p_j(\{\zeta\},\{H_{vv}\},\{k\}) - p_j^{\mathrm{ref}}\right]^2 \qquad (4.1)$$

where $p_j(\{\zeta\},\{H_{vv}\},\{k\})$ is the system's property of interest, p_j^{ref} the target value for that property and ω_j the relative weight of the j^{th} constraint. As shown in equation 4.1, the cost function f and the property p_j depend on the semiempirical parameters sets $\{\zeta\},\{H_{vv}\},\{k\}$. For each optimization run, it is possible to selectively optimize one or more of these parameters, for each atom in the molecule.

For the purpose of this work, the constraints are applied only to the energy values of the highest occupied molecular orbital (HOMO), the lowest and the second lowest unoccupied molecular orbital (LUMO and LUMO+1) of T-AM. The shifted DFT energies are used as target values. To evaluate the quality of the optimized EH parameters, the DFT/B3LYP and the EH orbitals are compared both in terms of their energy and their localization.

The optimization of the atomic parameters for amide and carboxylic groups is treated separately from the remaining C, N and O atoms in the molecule. In this way, specific sets of parameters are generated for those atoms, to account for

differences in chemical environments. Although this enlarges the basis set used for the calculations, it increases the accuracy of the results.

4.2.2. Quantum-classical dynamics of hole / electron wavepackets

In this chapter, the coherent mixing of the charge transfer state into the excitonic state is studied by combining quantum dynamics for the electrons, and classical molecular dynamics for the nuclei[42–44].

The time evolution of the electronic wavepacket, under the influence of the underlying nuclear dynamics, is carried out through the combined AO/MO time-propagation method[45]. This propagation method is outlined in **Scheme 4.2,** and proceeds as follows.

The position dependent AOs used to write the initial wavepacket $\Psi^{\mathrm{AO}}(t)$, for $t = 0$

$$\left|\Psi^{\mathrm{AO}}(0)\right\rangle = \sum_{\varphi}^{\mathrm{AO}} c_{\varphi}(0)\,|\varphi(0)\rangle \tag{4.2}$$

yield the Hückel Hamiltonian matrix elements $H_{\nu\mu}(0)$. The Hamiltonian changes between consecutive nuclear configurations through the overlap matrix, due to the position-dependent nature of the atomic orbital basis.

Diagonalization of this Hamiltonian matrix by means of the transformation operator

$$\hat{P}^{T} = \sum_{\psi}^{\mathrm{MO}} \sum_{\varphi,\chi}^{\mathrm{AO}} |\psi\rangle\langle\psi|\varphi\rangle\left(S_{\varphi\chi}^{-1}\right)\langle\varphi| \tag{4.3}$$

produces the adiabatic basis of delocalized molecular orbitals $\{\psi(0)\}$ at $t = 0$ (see **Scheme 4.2** , blue arrow $\hat{P}^{T}(0)$).

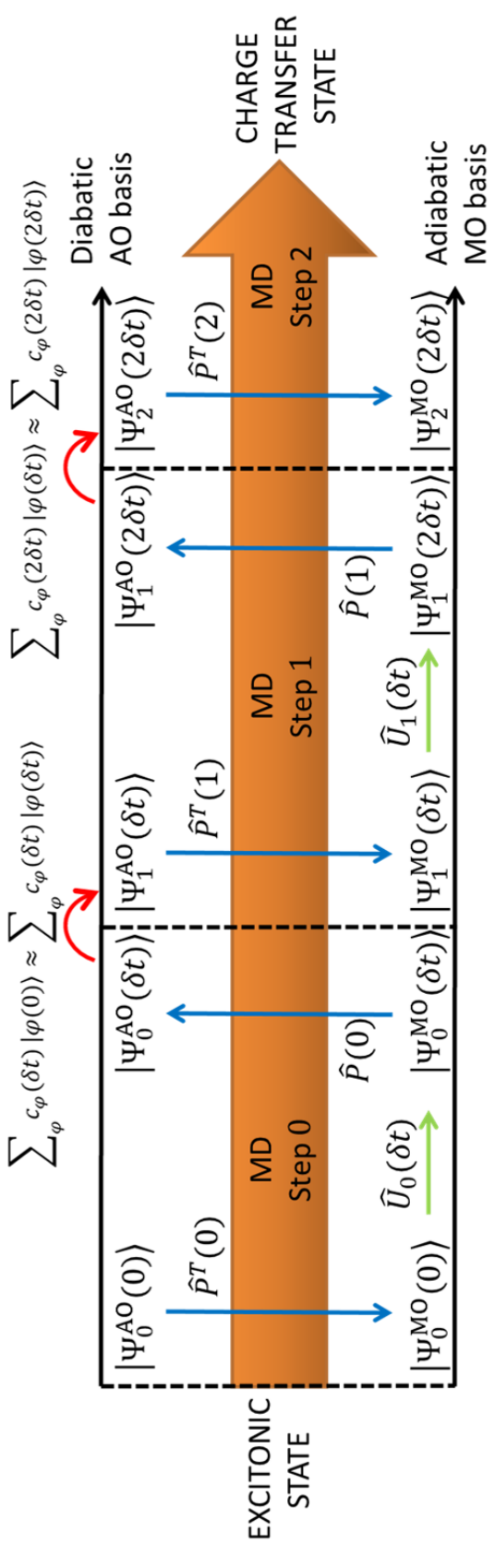

Scheme 4.2. Schematic representation of the AO/MO time propagation method, readapted from Ref.[49]. The straight arrows represent the operators $\hat{P}^T$, $\hat{P}$ (blue), and $\hat{U}$ the time propagator, green) acting on the wavepacket Ψ(t). The wavepacket' apices AO and MO indicate whether the wavepacket is expressed in terms of atomic or molecular orbitals; the subscript numbers indicate the MD step (nuclear geometry) to which correspond the AOs used to write the wavefunction. The red arrows, connecting different MD steps, describe the transferring of the wavepacket coefficients between consecutive time slices.

The wavepacket is then expressed in the orthonormal MO basis set according to

$$\left|\Psi^{\mathrm{MO}}(0)\right\rangle = \sum_{\psi}^{MO} C_{\psi}(0)\,|\psi(0)\rangle \ . \tag{4.4}$$

The advantage of using the molecular orbital representation is given by the simple form of the time-propagation equations, within a time slice δt.

In this basis, the time-propagation of the wavepacket is performed by solving the time-dependent Schrödinger equation

$$i\hbar\frac{d}{dt}|\Psi^{\mathrm{MO}}(t)\rangle = \widehat{H}(t)|\Psi^{\mathrm{MO}}(t)\rangle \ . \tag{4.5}$$

Within the time slice δt, since the nuclear geometry is treated as static, the molecular orbitals are time-independent $\left(\langle\psi|\dot{\psi}_i\rangle = 0\right)$. It follows that the solution of equation 4.5, within a time slice δt, leads to the time evolution of the MO coefficients as

$$C_{\psi}(t) = C_{\psi}(0)\exp(-iE_{\psi}\,t/\hbar) \ . \tag{4.6}$$

In the MO basis the Hamiltonian is diagonal and E_{ψ} are its eigenvalues. From equation 4.6 it is clear that within the time slice, the time evolution is contained only in the phase factor. This time-propagation step is indicated in **Scheme 4.2** by the green arrow.

Once $|\Psi^{\mathrm{MO}}(\delta t)\rangle$ has been obtained, the wavepacket is transformed back to the AO basis by using the transformation operator

$$\hat{P} = \sum_{\psi}^{\mathrm{MO}}\sum_{\varphi,\chi}^{\mathrm{AO}}|\varphi\rangle\left(S_{\varphi\chi}^{-1}\right)\langle\chi|\psi\rangle\,\langle\psi| \ , \tag{4.7}$$

as indicated with the blue arrows $\hat{P}(0)$ in **Scheme 4.2**.

This transformation is done since it is easier to transfer the wavepacket coefficients between time slices within the AO basis.

If δt is sufficiently small, we can reasonably assume that

$$\sum_{\varphi}^{AO} c_{\varphi}(\delta t)\,|\varphi(0)\rangle \approx \sum_{\varphi}^{AO} c_{\varphi}(\delta t)\,|\varphi(\delta t)\rangle\,, \tag{4.8}$$

which allows the transfer of $\{c_{\varphi}(\delta t)\}$ to the next nuclear configuration, as indicated by the red arrow bridging step 0 and step 1 in **Scheme 4.2**. However, as an effect of the nuclear motion, the center of the AO basis will change between consecutive MD steps yielding $H_{\nu\mu}(0) \neq H_{\nu\mu}(\delta t)$.

The procedure explained for MD step 0, is reiterated along the whole trajectory.

In this investigation, to simulate the initial excitonic state induced in the terrylene dye by photo excitation (t=0), the wavepackets for the hole and the electron are set to the HOMO and the LUMO of the adsorbate molecule, respectively. Consequently, $\Psi(0)$ is the exciton reactant state localized on the donor. However, along the dynamics, the wavepacket evolves into the charge transfer product state by delocalizing between the donor and the acceptor.

The nuclear trajectory for the isolated molecule, used for the time-evolution of the wavepackets, is calculated beforehand through *ab initio* Molecular Dynamics using the Car-Parrinello MD (CPMD) code[46] (see section 2.4 of this thesis). The DFT/B3LYP optimized geometry is used as the starting point for the MD simulation, which is carried out in vacuum using the pseudopotentials of reference[47] with a plane wave cut-off of 70 Rydberg and the BLYP[48,49] exchange correlation functional. Applying the Nosé-Hoover thermostat, the T-AM molecule is brought to a temperature of 300 K and allowed to equilibrate for 2 ps using a time step of $\delta t = 0.1$ fs. During the whole simulation, the atoms of the carboxylic acid anchoring group are constrained in their initial positions. At the end of the simulation the carboxylic acid is replaced with the previously optimized TiO_2 slab already functionalized with the anchoring unit.

Once the nuclear trajectory is obtained for the chromophore, the hole and the electron wavepackets are propagated along this trajectory following the combined AO/MO time-propagation method[44,16] described above, using the same time step of the MD simulation.

This methodology allows to treat the nonadiabatic transfer from an exciton reactant state to a charge transfer product state in the adiabatic MO representation through periodic projections onto the diabatic AO basis immediately followed by back transformation to the MO basis where the quantum electron dynamics is most conveniently performed. It has been already applied successfully for the description of heterogeneous electron transfer processes[42,50,45].

4.2.3. Normal mode analysis

The normal mode analysis for the isolated AM bridge unit is performed making use of the ADF software package[51–53]. The structure of the Phenyl-Amide-Phenyl molecule, initially optimized in vacuum at the DFT/B3LYP level, is subsequently used to numerically calculate the vibrational frequencies using the same computational set up.

4.3. RESULTS AND DISCUSSION

4.3.1. The optimized EH parameters

Following the procedure described in section 4.2.1, the DFT/B3LYP optimized structure and orbital energies of T-AM are used to carry on the optimization of the EH parameters. The results of the calculations performed with the semiempirical and the *ab initio* methods are compared in **Table 4.1**.

	DFT/B3LYP (eV)	Target values (eV)	Optimized EH (eV)
HOMO	**-4. 7**	**-10.7**	**-10.7**
	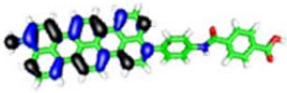		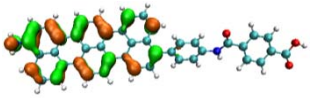
LUMO	**-2.6**	**-8.6**	**-8.6**
	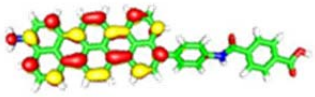		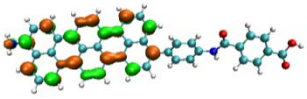
LUMO+1	**-2.4**	**-8.4**	**-8.3**
	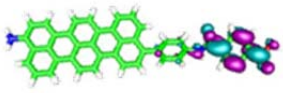		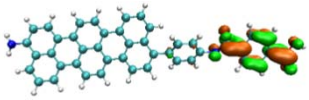

Table 4.1. Comparison between the frontier molecular orbital (FMO) energies obtained with the DFT/B3LYP method, the target values for the EH parameters optimizations, and the FMO energies calculated with the optimized EH parameters. The target values are estimated by applying a rigid 6 eV down shift to the DFT/B3LYP energy values. The images of the FMOs obtained for T-AM with DFT/B3LYP and the optimized EH parameters are shown for comparison.

The results clearly show that the generated set of optimized EH parameters are able to accurately reproduce the shape and the energy of the T-AM frontier molecular orbitals computed at the DFT/B3LYP level. This validates the use of this newly optimized basis set for the description of T-AM electronic properties and for studying the electron quantum dynamics processes.

4.3.2. Electron quantum dynamics simulations

The optimized EH parameters are used to perform a single point calculation of the entire chromophore/semiconductor system.

In **Figure 4.1a** the total density of the unoccupied states of T-AM-TiO_2 projected on the chromophore (Dye, in blue) and on the semiconductor (TiO_2, in grey) are compared.

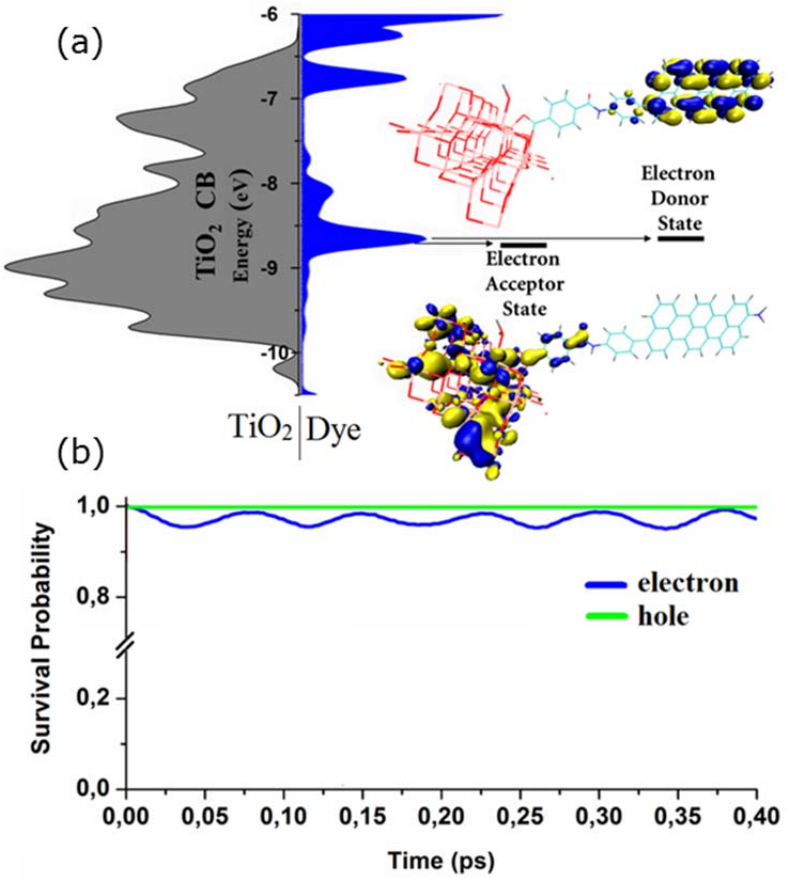

Figure 4.1. **(a)** Comparison between the density of the chromophore unoccupied states (Dye, in blue) and of the TiO_2 conduction band (TiO_2, in grey). On the right hand side, the electron donor and acceptor states contributing to the peak around -8.7 eV are represented. **(b)** Electron and hole time-dependent SP profiles of system T-AM-TiO_2 in the absence of nuclear motion (blue and green line, respectively). The time step of the simulation is $\delta\tau$=0.1 fs. Both calculations are performed for the entire T-AM-TiO_2 system on the fixed set of ground-state optimized molecular coordinates using the optimized EH parameters.

To prepare the system, the T-AM structure employed for the parametrization of the EH Hamiltonian is used. The projected density of states for T-AM (**Figure 4.1a**, Dye) presents a peak at -8.7 eV. This peak is associated with the two almost degenerate ($\Delta\varepsilon$ = -0.05 eV) unoccupied system orbitals shown in **Figure 4.1a**. These two orbitals, labeled Electron Donor (ED) and Electron Acceptor (EA) states,

correspond respectively to the LUMO and LUMO+1 of the isolated dye molecule (**Table 4.1**).

An electron quantum dynamics simulation (EQD) is performed for the T-AM-TiO_2 system over the same set of nuclear coordinates used for the DOS calculation, keeping the nuclear positions fixed. Since the photoexcitation of the dye populates the molecular orbital localized on the terrylene (ED), the photoexcited electron has to travel across the bridge through the EA state to reach the TiO_2 surface. Despite the proximity between the electron donor and acceptor states and the presence of a thermodynamic driving force, no ET from T-AM to TiO_2 is observed within the 2 ps EQD simulation in absence of nuclear motion (see **Figure 4.1b**).

To investigate the effect of the nuclear motion on the electron dynamics the hole/electron quantum dynamics calculations are repeated by evolving the wavepackets over a classical MD trajectory obtained beforehand (see section 4.2.2)[54,55]. Since we use a nuclear trajectory obtained in the ground state, the effect of the thermal relaxation of the photogenerated hot exciton is not included. However, since this effect is fast and highly localized on the antenna, it is not expected to significantly affect the dynamics of the ET on a longer time scale[6] (see section 4.6.1 in the Appendix). The results of the electron quantum dynamics performed along the MD trajectory are reported in **Figure 4.2** showing the survival probability (SP) of the electron wavepacket. The SP is defined as the time-dependent population of the wavepacket within the dye[42]. When the wavepacket is fully localized within the sensitizer SP=1, while SP=0 when it is fully transferred to TiO_2.

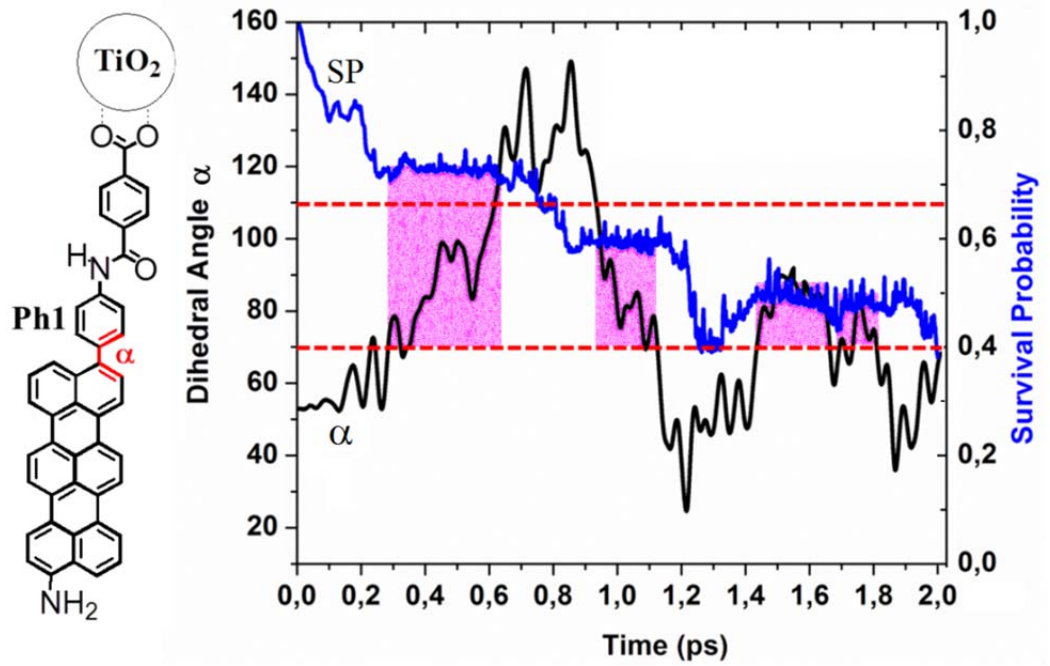

Figure 4.2. Electron quantum dynamics simulation of the T-AM-TiO_2 system (SP, blue) along a classic MD trajectory obtained with CPMD. The electron and nuclear dynamics both employ a time step δt=0.1 fs. A schematic representation of the analyzed complex is presented on the left hand side of the figure, together with the identification of the dihedral angle α (in red). The black line (α) represents the variation of this angle along the dynamics. The range of values identified as crucial for electron injection is delimited by the red dashed lines. The regions highlighted in pink correspond to time intervals in which the dihedral angle α falls within this range.

The survival probability profile (**Figure 4.2,** SP) shows that the introduction of nuclear dynamics induces significant ET within the first few hundreds fs, in contrast to the results for T-AM-TiO_2 without nuclear dynamics (**Figure 4.1b)**. This demonstrates the importance of the coupling between the electron dynamics and thermal motions in the description of ET processes.

Additionally, the SP profile is characterized by the presence of plateaus emerging periodically every ~250 fs indicating that the electron injection is temporarily quenched. At the same time the SP evolution shows that back charge transfer from the semiconductor on the terrylene antenna does not occur, well in line with the rectifier property of the AM bridge (see section 4.6.2 in the Appendix). The analysis of the molecular dynamics trajectory reveals a correlation between the recurrence of these plateaus and the fluctuation of the dihedral angle α (**Figure 4.2**, black line), defined between the terrylene and the phenyl ring Ph1 (see **Figure 4.2**, left). The electron injection occurs only when α<70º or α>110º (red dashed lines in **Figure 4.2**). On the contrary, if 70º<α<110º the transfer is hindered (areas highlighted in

pink, **Figure 4.2**). The variation of the dihedral angle α influences the delocalization of the electron donor state over the Ph1 ring, as shown in **Figure 4.3**.

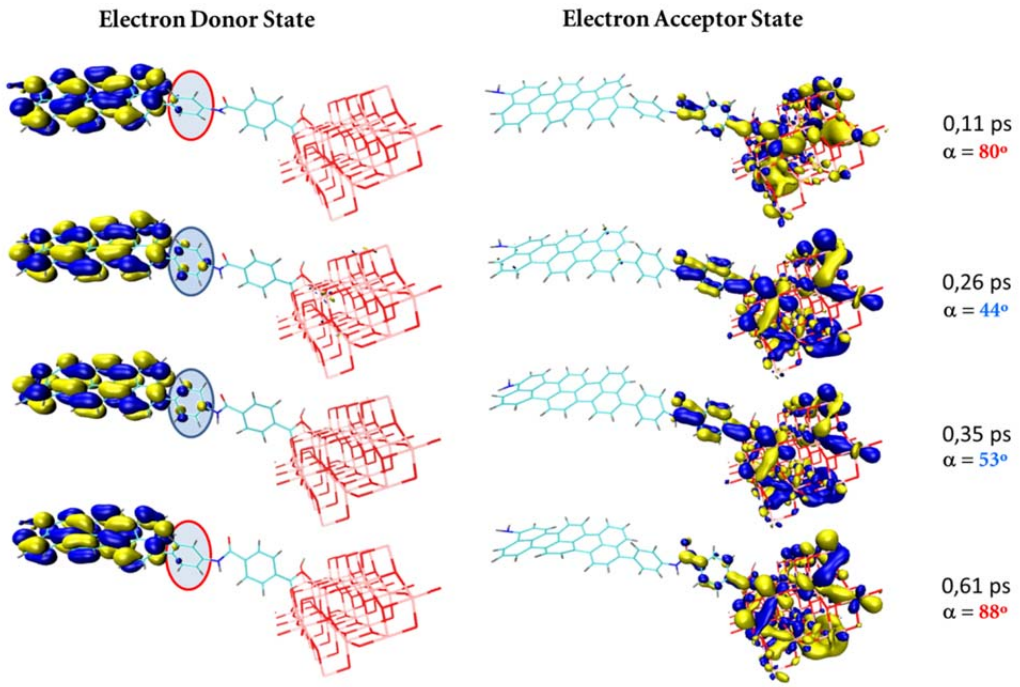

Figure 4.3. Localization of the Electron Donor and Electron Acceptor states along the T-AM-TiO_2 MD trajectory. On the right hand side are reported the MD time frames and the value of the dihedral angle α corresponding to the two electronic states shown.

When 70º<α<110º the ED state is confined on the antenna (T) and is separated from the electron acceptor orbital by the Ph1 ring (red circles in **Figure 4.3**). However, when α is outside the aforementioned range the planarity and consequently the conjugation between Ph1 and the terrylene is increased. This induces the delocalization of the ED state over Ph1 (blue circles in **Figure 4.3**) and thus transiently enhances the coupling between the donor and acceptor states.

It is worth pointing out that performing the electron quantum dynamics while keeping the nuclei fixed, does not show electron injection on a timescale of a few ps, even when geometries with α values outside the 70°-110° range extracted from the previous trajectory are used (as already shown in **Figure 4.1b** for the initial geometry, α≈50º). This indicates that ET is not solely promoted by a proper value of α, but instead requires the coupling with other specific vibrational modes[56]. To identify those we use the same nuclear trajectory to perform an EQD starting from the molecular configuration at 890 fs with α =123º (**Figure 4.2**, just before the second shaded region). The results are presented in **Figure 4.4b**.

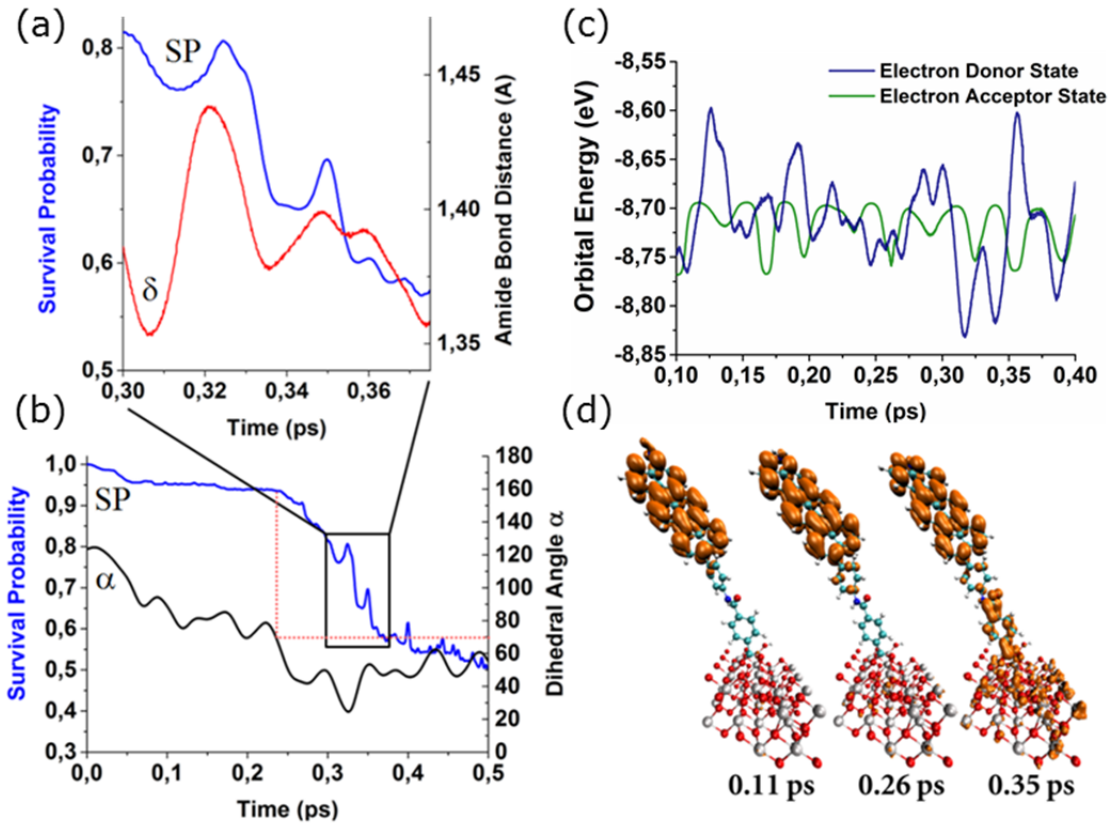

Figure 4.4. **(a)** Comparison between the survival probability (SP, blue line) oscillations and the amide bond (C-N) distance (δ, red line) along the EQD. **(b)** Comparison between the electron injection profile (SP, blue line) and the variation of the dihedral angle (α, black line) along the EQD simulation for the T-AM-TiO_2 system. The red dotted lines correlate the starting of the electron injection with the decrease of α below 70°. **(c)** Energy values of the Electron Donor and the Electron Acceptor states along a portion of the EQD simulation. **(d)** Snapshots extracted along the EQD trajectory representing the electron wavepacket traveling through the bridge.

Initially, while α>110º, a limited injection (5%) is observed within the first ~50 fs. This transient is followed by a plateau up to about 230 fs, corresponding to the period during which 70º<α<110º. Then ET towards the TiO_2 is resumed by the decrease of α below the 70° threshold (red dotted lines in **Figure 4.4b**) and is characterized by electron density fluctuations with a period of ~30 fs (**Figure 4.4b**, black rectangle). The Fourier analysis of these rapid fluctuations gives a broad peak centered at ~1250 cm^{-1} (see **Table 4.2a**).

In **Figure 4.4a** it is shown that the oscillations characteristic of the electron injection (SP, blue line) are highly correlated with the variation of the amide bond distance N-C (δ, red line). A normal mode analysis of the AM bridge shows that the N-C bond length is modulated by the normal modes ω_1 (1090 cm^{-1}) and ω_2 (1226

cm^{-1}) reported in **Table 4.2a**. In fact, as described in **Table 4.2b**, these modes involve mostly the variation of the γ, δ and ε bonds localized at the interface between the ED and EA orbitals (**Table 4.2**).

(a)

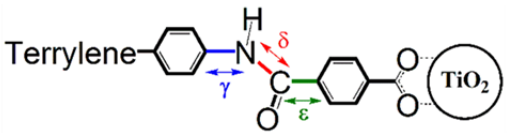

Fourier analysis of SP:	**1250 cm^{-1}**
Symmetric stretching of δ and ε (ω_1):	**1090 cm^{-1}**
Antisymmetric stretching of γ and δ (ω_2):	**1226 cm^{-1}**

(b)

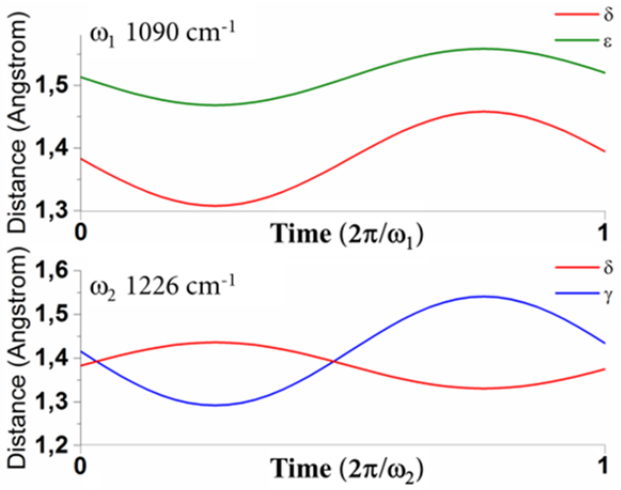

Table 4.2. **(a)** Frequencies of relevant normal modes of the AM bridge (ω_1 and ω_2.) compared with the frequency obtained from the Fourier analysis of the electron injection oscillations along the EQD trajectory. γ, δ and ε are the three bonds showing a major contribution to the normal modes ω_1 and ω_2. **(b)** Graphic representation of the . γ, δ and ε bond distance variations associated to the normal modes ω_1 and ω_2.

The energy fluctuations of these two orbitals are represented in **Figure 4.4c** for a segment of the MD trajectory (0.1-0.4 ps), characteristic of the whole simulation. The energies of EA and ED MO states constantly cross each other, which confirms the nonadiabatic character of the electron transfer process. The crossing also shows that the primary ET step and the rectification do not require a strong energy gradient to take place. The ED and EA states oscillate with distinctive frequencies of 1100 cm^{-1} and 1235 cm^{-1}, respectively. The remarkable similarity between these two values and the frequencies of the normal modes ω_1 (1090 cm^{-1}) and ω_2 (1226 cm^{-1}) strongly indicates the influence of these particular vibrations on the energies of the electron donor and acceptor states. Overall these results underline the importance of these specific nuclear vibrations in driving the electron injection. Similar evidence of vibronic coupling effects have been recently reported for different organic supramolecular complexes[28,30,57].

Quantum coherent conversion from an excitonic state to a charge transfer state requires that the two states partially occupy the same volume, and that their energy

levels are close enough to be coherently coupled by vibrational modes[31–33,58–60]. In the system discussed here, the two states involved in the electron transfer are associated with orbitals that initially are sufficiently close in energy but spatially separated. Thermal motion brings a conformational change (variation of α) that makes them partially occupy the same molecular region. Under this condition the two states can be coherently coupled by the fast vibrational modes localized at their interface, thus allowing the propagation of the electronic wavepacket by a convergence of electronic and nuclear dynamics.

A visual representation of the electron wavepacket propagating across the system is reported in **Figure 4.4d**. These snapshots clearly show how the wavepacket propagates through a channel which is opened as a result of the Ph1 rotation. The snapshot at t=0.35 ps shows clearly that the wavepacket can be described as a superposition of the corresponding ED and EA states shown in **Figure 4.3**. This demonstrates that the electron transfer is proceeding gradually from the ED state to the EA state, rather than through an instantaneous hopping. The MD trajectory is calculated separately and cannot change in response to the QED to produce electron-nuclear resonance[57]. Nevertheless, quantum dynamics always selects the fastest channel to the product making the electronic system acting as a phonon antenna. That is, it selects the vibrational mode that is "just right" to facilitate coherent transfer[60]. This validates the coupled quantum classical approach of treating the nonadiabatic transfer between two states through periodic instantaneous rearrangement of nuclear positions in the diabatic AO base, while performing the propagation in the adiabatic MO base.

4.4. CONCLUSIONS

In summary, efficient ET in T-AM-TiO_2 is driven by a strong coupling between the electron dynamics and specific nuclear vibrational modes. It has been shown that a slow rotation of the bridge with respect to the antenna opens a preferential channel for ET by changing the localization of the donor and acceptor states. When the channel is open, the charge can move across the bridge from the electron donor to the acceptor state driven by the bridge vibrational modes that induce periodic crossing of energy levels and nonadiabatic coupling of these two states.

These results underline the importance of including the nuclear dynamics for a proper description of the electron injection. In addition, I have verified the rectification properties of the AM bridge as part of a chromophore for a DSSC. The vibrational modes identified through the analysis of the correlation between nuclear and electron dynamics provide possible strategies for accelerating the electron injection process for high efficiency by *e.g.* structural modifications of the AM bridge to constrain rotations of the Ph1 ring.

4.5. REFERENCES

(1) O'Regan, B.; Grätzel, M. A Low-Cost, High-Efficiency Solar Cell Based on Dye-Sensitized Colloidal TiO_2 Films. *Nature* **1991**, *353* (6346), 737–740.

(2) Duncan, W. R.; Craig, C. F.; Prezhdo, O. V. Time-Domain Ab Initio Study of Charge Relaxation and Recombination in Dye-Sensitized TiO_2. *J. Am. Chem. Soc.* **2007**, *129* (27), 8528–8543.

(3) Listorti, A.; O'Regan, B.; Durrant, J. R. Electron Transfer Dynamics in Dye-Sensitized Solar Cells. *Chem. Mater.* **2011**, *23* (15), 3381–3399.

(4) Nattestad, A.; Mozer, A. J.; Fischer, M. K. R.; Cheng, Y.-B.; Mishra, A.; Bäuerle, P.; Bach, U. Highly Efficient Photocathodes for Dye-Sensitized Tandem Solar Cells. *Nat. Mater.* **2010**, *9* (1), 31–35.

(5) Zhou, N.; Lin, H.; Lou, S. J.; Yu, X.; Guo, P.; Manley, E. F.; Loser, S.; Hartnett, P.; Huang, H.; Wasielewski, M. R.; et al. Morphology-Performance Relationships in High-Efficiency All-Polymer Solar Cells. *Adv. Energy Mater.* **2014**, *4* (3), n/a – n/a.

(6) Hagfeldt, A.; Boschloo, G.; Sun, L.; Kloo, L.; Pettersson, H. Dye-Sensitized Solar Cells. *Chem. Rev.* **2010**, *110* (11), 6595–6663.

(7) Monti, A.; de Groot, H. J. M.; Buda, F. In-Silico Design of a Donor–Antenna–Acceptor Supramolecular Complex for Photoinduced Charge Separation. *J. Phys. Chem. C* **2014**, *118* (29), 15600–15609.

(8) Haid, S.; Marszalek, M.; Mishra, A.; Wielopolski, M.; Teuscher, J.; Moser, J.-E.; Humphry-Baker, R.; Zakeeruddin, S. M.; Grätzel, M.; Bäuerle, P. Significant Improvement of Dye-Sensitized Solar Cell Performance by Small Structural Modification in Π-Conjugated Donor–Acceptor Dyes. *Adv. Funct. Mater.* **2012**, *22* (6), 1291–1302.

(9) Caprasecca, S.; Mennucci, B. Excitation Energy Transfer in Donor-Bridge-Acceptor Systems: A Combined Quantum-Mechanical/Classical Analysis of the Role of the Bridge and the Solvent. *J. Phys. Chem. A* **2014**, *118* (33), 6484–6491.

(10) Ma, W.; Jiao, Y.; Meng, S. Modeling Charge Recombination in Dye-Sensitized Solar Cells Using First-Principles Electron Dynamics: Effects of Structural Modification. *Phys. Chem. Chem. Phys.* **2013**, *15* (40), 17187–17194.

(11) Ambrosio, F.; Martsinovich, N.; Troisi, A. What Is the Best Anchoring Group for a Dye in a Dye-Sensitized Solar Cell? *J. Phys. Chem. Lett.* **2012**, *3* (11), 1531–1535.

(12) Koops, S. E.; O'Regan, B. C.; Barnes, P. R. F.; Durrant, J. R. Parameters Influencing the Efficiency of Electron Injection in Dye-Sensitized Solar Cells. *J. Am. Chem. Soc.* **2009**, *131* (13), 4808–4818.

(13) Meng, S.; Kaxiras, E. Electron and Hole Dynamics in Dye-Sensitized Solar Cells: Influencing Factors and Systematic Trends. *Nano Lett.* **2010**, *10* (4), 1238–1247.

(14) De Angelis, F. Modeling Materials and Processes in Hybrid/Organic Photovoltaics: From Dye-Sensitized to Perovskite Solar Cells. *Acc. Chem. Res.* **2014**, *47* (11), 3349–3360.

(15) De Angelis, F.; Fantacci, S.; Selloni, A.; Nazeeruddin, M. K.; Grätzel, M. Time-Dependent Density Functional Theory Investigations on the Excited States of Ru(II)-Dye-Sensitized TiO2 Nanoparticles: The Role of Sensitizer Protonation. *J. Am. Chem. Soc.* **2007**, *129* (46), 14156–14157.

(16) Nieto-Pescador, J.; Abraham, B.; Gundlach, L. Photoinduced Ultrafast Heterogeneous Electron Transfer at Molecule–Semiconductor Interfaces. *J. Phys. Chem. Lett.* **2014**, *5* (20), 3498–3507.

(17) Zhu, H.; Yang, Y.; Hyeon-Deuk, K.; Califano, M.; Song, N.; Wang, Y.; Zhang, W.; Prezhdo, O. V.; Lian, T. Auger-Assisted Electron Transfer from Photoexcited Semiconductor Quantum Dots. *Nano Lett.* **2014**, *14* (3), 1263–1269.

(18) Akimov, A. V.; Neukirch, A. J.; Prezhdo, O. V. Theoretical Insights into Photoinduced Charge Transfer and Catalysis at Oxide Interfaces. *Chem. Rev.* **2013**, *113* (6), 4496–4565.
(19) Akimov, A. V.; Prezhdo, O. V. Nonadiabatic Dynamics of Charge Transfer and Singlet Fission at the Pentacene/C60 Interface. *J. Am. Chem. Soc.* **2014**.
(20) Tafen, D. N.; Long, R.; Prezhdo, O. V. Dimensionality of Nanoscale TiO_2 Determines the Mechanism of Photoinduced Electron Injection from a CdSe Nanoparticle. *Nano Lett.* **2014**, *14* (4), 1790–1796.
(21) Long, R.; English, N. J.; Prezhdo, O. V. Minimizing Electron–Hole Recombination on TiO_2 Sensitized with PbSe Quantum Dots: Time-Domain Ab Initio Analysis. *J. Phys. Chem. Lett.* **2014**, 2941–2946.
(22) Aviram, A.; Ratner, M. A. Molecular Rectifiers. *Chem. Phys. Lett.* **1974**, *29* (2), 277–283.
(23) Ding, W.; Negre, C. F. A.; Vogt, L.; Batista, V. S. Single Molecule Rectification Induced by the Asymmetry of a Single Frontier Orbital. *J. Chem. Theory Comput.* **2014**, *10* (8), 3393–3400.
(24) Ding, W.; Negre, C. F. A.; Palma, J. L.; Durrell, A. C.; Allen, L. J.; Young, K. J.; Milot, R. L.; Schmuttenmaer, C. A.; Brudvig, G. W.; Crabtree, R. H.; et al. Linker Rectifiers for Covalent Attachment of Transition-Metal Catalysts to Metal-Oxide Surfaces. *ChemPhysChem* **2014**, *15* (6), 1138–1147.
(25) Fleury, L.; Zumbusch, A.; Orrit, M.; Brown, R.; Bernard, J. Spectral Diffusion and Individual Two-Level Systems Probed by Fluorescence of Single Terrylene Molecules in a Polyethylene Matrix. *J. Lumin.* **1993**, *56* (1–6), 15–28.
(26) Harms, G. S.; Irngartinger, T.; Reiss, D.; Renn, A.; Wild, U. P. Fluorescence Lifetimes of Terrylene in Solid Matrices. *Chem. Phys. Lett.* **1999**, *313* (3–4), 533–538.
(27) Edvinsson, T.; Pschirer, N.; Schöneboom, J.; Eickemeyer, F.; Boschloo, G.; Hagfeldt, A. Photoinduced Electron Transfer from a Terrylene Dye to TiO_2: Quantification of Band Edge Shift Effects. *Chem. Phys.* **2009**, *357* (1–3), 124–131.
(28) Andrea Rozzi, C.; Maria Falke, S.; Spallanzani, N.; Rubio, A.; Molinari, E.; Brida, D.; Maiuri, M.; Cerullo, G.; Schramm, H.; Christoffers, J.; et al. Quantum Coherence Controls the Charge Separation in a Prototypical Artificial Light-Harvesting System. *Nat. Commun.* **2013**, *4*, 1602.
(29) Chapman, C. T.; Liang, W.; Li, X. Ultrafast Coherent Electron–Hole Separation Dynamics in a Fullerene Derivative. *J. Phys. Chem. Lett.* **2011**, *2* (10), 1189–1192.
(30) Falke, S. M.; Rozzi, C. A.; Brida, D.; Maiuri, M.; Amato, M.; Sommer, E.; Sio, A. D.; Rubio, A.; Cerullo, G.; Molinari, E.; et al. Coherent Ultrafast Charge Transfer in an Organic Photovoltaic Blend. *Science* **2014**, *344* (6187), 1001–1005.
(31) Romero, E.; Augulis, R.; Novoderezhkin, V. I.; Ferretti, M.; Thieme, J.; Zigmantas, D.; van Grondelle, R. Quantum Coherence in Photosynthesis for Efficient Solar-Energy Conversion. *Nat. Phys.* **2014**, *10* (9), 676–682.
(32) Chin, A. W.; Prior, J.; Rosenbach, R.; Caycedo-Soler, F.; Huelga, S. F.; Plenio, M. B. The Role of Non-Equilibrium Vibrational Structures in Electronic Coherence and Recoherence in Pigment-Protein Complexes. *Nat. Phys.* **2013**, *9* (2), 113–118.
(33) Fuller, F. D.; Pan, J.; Gelzinis, A.; Butkus, V.; Senlik, S. S.; Wilcox, D. E.; Yocum, C. F.; Valkunas, L.; Abramavicius, D.; Ogilvie, J. P. Vibronic Coherence in Oxygenic Photosynthesis. *Nat. Chem.* **2014**, *6* (8), 706–711.
(34) Hayes, D.; Griffin, G. B.; Engel, G. S. Engineering Coherence among Excited States in Synthetic Heterodimer Systems. *Science* **2013**, *340* (6139), 1431–1434.
(35) Hoffmann, R. An Extended Hückel Theory. I. Hydrocarbons. *J. Chem. Phys.* **1963**, *39* (6), 1397–1412.

(36) Ammeter, J. H.; Buergi, H. B.; Thibeault, J. C.; Hoffmann, R. Counterintuitive Orbital Mixing in Semiempirical and Ab Initio Molecular Orbital Calculations. *J. Am. Chem. Soc.* **1978**, *100* (12), 3686–3692.
(37) Wolfsberg, M.; Helmholz, L. The Spectra and Electronic Structure of the Tetrahedral Ions MnO_4^-, CrO_4^{--}, and ClO_4^-. *J. Chem. Phys.* **1952**, *20* (5), 837–843.
(38) Santiago Alvarez. Table of Parameters for Extended Huckel Calculations, Collected by Santiago Alvarez, Universitat de Barcelona (1995). **1995**.
(39) Becke, A. D. Density-functional Thermochemistry. III. The Role of Exact Exchange. *J. Chem. Phys.* **1993**, *98* (7), 5648–5652.
(40) M. J. Frisch, G. W. Trucks, H. B. Schlegel, G. E. Scuseria, M. A. Robb, J. R. Cheeseman, G. Scalmani, V. Barone, B. Mennucci, G. A. Petersson, et al. *Gaussian 09, Revision D.01*; Gaussian, Inc.: Wallingford CT, 2009.
(41) Ding, W.-L.; Wang, D.-M.; Geng, Z.-Y.; Zhao, X.-L.; Yan, Y.-F. Molecular Engineering of Indoline-Based D–A–π–A Organic Sensitizers toward High Efficiency Performance from First-Principles Calculations. *J. Phys. Chem. C* **2013**, *117* (34), 17382–17398.
(42) Hoff, D. A.; da Silva, R.; Rego, L. G. C. Coupled Electron–Hole Quantum Dynamics on D−π–A Dye-Sensitized TiO_2 Semiconductors. *J. Phys. Chem. C* **2012**, *116* (40), 21169–21178.
(43) Rego, L. G. C.; Hames, B. C.; Mazon, K. T.; Joswig, J.-O. Intramolecular Polarization Induces Electron–Hole Charge Separation in Light-Harvesting Molecular Triads. *J. Phys. Chem. C* **2014**, *118* (1), 126–134.
(44) Hoff, D. A.; Silva, R.; Rego, L. G. C. Subpicosecond Dynamics of Metal-to-Ligand Charge-Transfer Excited States in Solvated $[Ru(bpy)_3]^{2+}$ Complexes. *J. Phys. Chem. C* **2011**, *115* (31), 15617–15626.
(45) Da Silva, R.; Hoff, D. A.; Rego, L. G. C. Coupled Quantum-Classical Method for Long Range Charge Transfer: Relevance of the Nuclear Motion to the Quantum Electron Dynamics. *J. Phys. Condens. Matter* **2015**, *27* (13), 134206.
(46) *CPMD, Http://www.cpmd.org/, Copyright IBM Corp 1990-2008, Copyright MPI fürFestkörperforschung Stuttgart 1997-2001*.
(47) Lin, I.-C.; Coutinho-Neto, M. D.; Felsenheimer, C.; von Lilienfeld, O. A.; Tavernelli, I.; Rothlisberger, U. Library of Dispersion-Corrected Atom-Centered Potentials for Generalized Gradient Approximation Functionals: Elements H, C, N, O, He, Ne, Ar, and Kr. *Phys. Rev. B* **2007**, *75* (20), 205131.
(48) Becke, A. D. Density-Functional Exchange-Energy Approximation with Correct Asymptotic Behavior. *Phys. Rev. A* **1988**, *38* (6), 3098–3100.
(49) Lee, C.; Yang, W.; Parr, R. G. Development of the Colle-Salvetti Correlation-Energy Formula into a Functional of the Electron Density. *Phys. Rev. B* **1988**, *37* (2), 785–789.
(50) Abuabara, S. G.; Rego, L. G. C.; Batista, V. S. Influence of Thermal Fluctuations on Interfacial Electron Transfer in Functionalized TiO_2 Semiconductors. *J. Am. Chem. Soc.* **2005**, *127* (51), 18234–18242.
(51) Te Velde, G.; Bickelhaupt, F. M.; Baerends, E. J.; Fonseca Guerra, C.; van Gisbergen, S. J. A.; Snijders, J. G.; Ziegler, T. Chemistry with ADF. *J. Comput. Chem.* **2001**, *22* (9), 931–967.
(52) Fan, L.; Ziegler, T. Application of Density Functional Theory to Infrared Absorption Intensity Calculations on Main Group Molecules. *J. Chem. Phys.* **1992**, *96* (12), 9005–9012.
(53) Fan, L.; Ziegler, T. Nonlocal Density Functional Theory as a Practical Tool in Calculations on Transition States and Activation Energies. Applications to Elementary Reaction Steps in Organic Chemistry. *J. Am. Chem. Soc.* **1992**, *114* (27), 10890–10897.
(54) Olbrich, C.; Strümpfer, J.; Schulten, K.; Kleinekathöfer, U. Theory and Simulation of the Environmental Effects on FMO Electronic Transitions. *J. Phys. Chem. Lett.* **2011**, *2* (14), 1771–1776.

(55) Akimov, A. V.; Prezhdo, O. V. Persistent Electronic Coherence Despite Rapid Loss of Electron–Nuclear Correlation. *J. Phys. Chem. Lett.* **2013**, *4* (22), 3857–3864.
(56) Jiao, Y.; Ding, Z.; Meng, S. Atomistic Mechanism of Charge Separation upon Photoexcitation at the Dye–semiconductor Interface for Photovoltaic Applications. *Phys. Chem. Chem. Phys.* **2011**, *13* (29), 13196–13201.
(57) Eisenmayer, T. J.; Buda, F. Real-Time Simulations of Photoinduced Coherent Charge Transfer and Proton-Coupled Electron Transfer. *ChemPhysChem* **2014**, *15* (15), 3258–3263.
(58) Eisenmayer, T. J.; Lasave, J. A.; Monti, A.; de Groot, H. J. M.; Buda, F. Proton Displacements Coupled to Primary Electron Transfer in the Rhodobacter Sphaeroides Reaction Center. *J. Phys. Chem. B* **2013**, *117* (38), 11162–11168.
(59) Eisenmayer, T. J.; de Groot, H. J. M.; van de Wetering, E.; Neugebauer, J.; Buda, F. Mechanism and Reaction Coordinate of Directional Charge Separation in Bacterial Reaction Centers. *J. Phys. Chem. Lett.* **2012**, *3* (6), 694–697.
(60) Purchase, R.L.; de Groot, H.J.M. Biosolar Cells: Global Artificial Photosynthesis Needs Responsive Matrices with Quantum Coherent Kinetic Control for High Yield. *Interface Focus* **2015**, *5*.

4.6. APPENDIX

4.6.1. Test on geometrical relaxation in the excited state

An additional test has been performed to check the effects of the photo-excitation on the T-AM chromophore. Using the Gaussian 09 software package[40], together with the CAM-B3LYP exchange-correlation functional and the cc-pVDZ basis set, we have optimized the geometry of the T-AM dye in the first excited state, which has predominant HOMO-LUMO character. The optimized geometry in the excited state shows only small changes in the C-C bond lengths of the terrylene antenna with maximum displacements of ~0.03 Å. Given that the LUMO is highly localized on the terrylene, it is not surprising that these geometrical changes are only observed in the terrylene molecule and do not propagate on the AM bridge whose geometry is essentially not modified by the excitation. These results strongly suggest that the dynamics of the AM bridge will be hardly affected by the excitation localized on the terrylene antenna, giving further justification to the use of a ground state dynamics for the study of the electron injection.

4.6.2. Test on T-Stilbene-TiO_2

The survival probability reported in **Figure 4.2** and **Figure 4.4** shows a constant decrease of the electron wavepacket localized on T-AM. This indicates the absence of large charge fluctuations from the semiconductor back onto the donor state of the dye. To verify that this is due to the AM bridge rectification properties, following the same computational procedure used for T-AM–TiO_2, we perform an EQD simulation for a system in which we substitute the AM bridge with the fully conjugated (E)-stilbene molecule (**Figure A4.1a**). Due to its conjugation this system is not expected to show rectification[23].

The results for T-Stilbene-TiO_2 are reported in **Figure A4.1b**. Due to the fully conjugated nature of (E)-stilbene, the initial wavepacket is localized not only on the terrylene but on the entire dye. In this case the electron injection is extremely fast, due to the strong coupling with the semiconductor conduction band states (see **Figure A4.1b**, first 20 fs). However, along the dynamics the survival probability for T-Stilbene-TiO_2 shows strong fluctuations associated with electron density fluctuation between the antenna and the semiconductor (see insets in **Figure A4.1b**). This is a strong indication that the T-Stilbene-TiO_2 system does not show rectification capability in contrast to the results shown for T-AM-TiO_2.

(a)

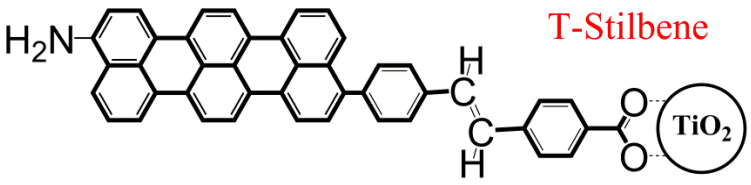

(b)

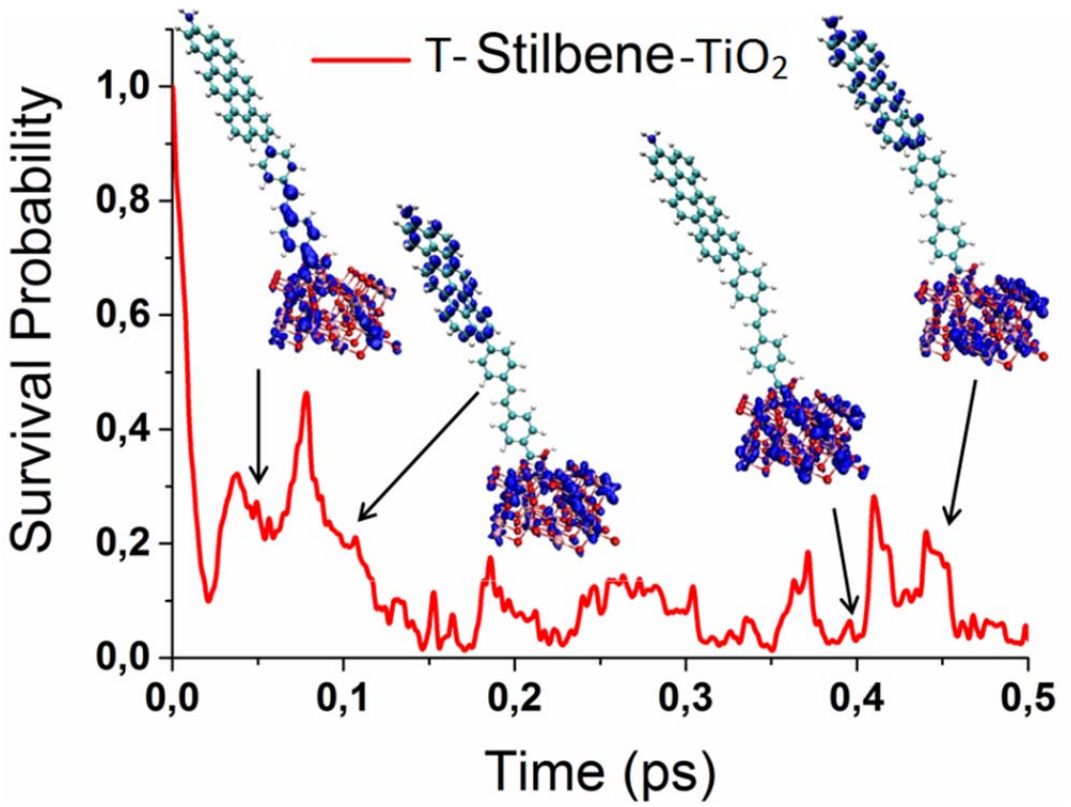

Figure A4.1. **(a)** Schematic representation of the T-Stilbene dye. **(b)** SP profile of the EQD simulation of T-Stilbene-TiO_2 along an MD trajectory. The insets show the wavepacket localization at different snapshots along the EQD.